Electronic Supplementary Material (ESI) for Materials Horizons.

Supplementary Materials for

Semiconductor to Topological Insulator Transition Induced by Stress Propagation in Metal Dichalcogenides Core-Shell Lateral Heterostructures

Xi Dong,[a] Wei Lai,[b] Pengpeng Zhang[*a]

[a]*Department of Physics and Astronomy, Michigan State University, East Lansing, MI 48824, USA*

[b]*Department of Chemical Engineering and Materials Science, Michigan State University, East Lansing, MI 48824, USA*

*Corresponding author: zhangpe@msu.edu

This file contains:

Methods

Discussion Sections: 1-7

Fig. S1 to S8

Methods

Experimental detail: WSe_2/$SnSe_2$ HSs were created on HOPG substrate via subsequent deposition of WSe_2 and $SnSe_2$ by MBE. Before deposition, HOPG substrate was freshly cleaved, cleaned with acetone and Isopropyl alcohol, and then immediately transferred into UHV with base pressure $<3\times10^{-10}$ mBar for degassing (up to ~650K for several hours). The pristine H-phase WSe_2 was grown at a rate of ~45 mins per monolayer by co-evaporation of pure W and Se using an E-beam evaporator and a cracker cell, respectively. The substrate was kept at ~723K during the deposition. $SnSe_2$ was subsequently deposited at a rate of ~2 hours per monolayer by co-evaporation of pure Sn and Se, again, using E-beam evaporator and cracker cell. To avoid decomposition of $SnSe_2$, the substrate was kept at ~438K. Chamber pressure of ~1×10^{-8} mBar was recorded during the MBE growth. WSe_2/$SnSe_2$ sample was then *in-situ* transferred into an inter-connected characterization chamber (base pressure $<3\times10^{-11}$mBar) which hosts an Omicron low temperature STM operated at liquid nitrogen temperature (~77.5K). STS curves were collected through a lock-in amplifier with the STM tip calibrated by measuring reference spectra on silver substrate to avoid tip artifacts. The modulation signal of the lock-in amplifier was set at 26meV in amplitude and 1kHz in frequency.

Computational detail: DFT calculations were performed by the cp2k[1, 2] package that employs mixed Gaussian and plane wave basis sets. The valence electron configurations were Sn ($5s^25p^2$), W ($5s^25p^65d^46s^2$), and Se ($4s^24p^4$) with Goedecker–Teter–Hutter (GTH) scalar-relativistic and norm-conserving pseudopotentials.[3, 4] The plane wave cutoff was 400 Ry and Gaussian basis sets were DZVP-MOLOPT-SR[5]. The exchange-correlation functionals was the dispersion-corrected revised Perdew-Burke-Ernzerhof with Becke-Johnson damping (revPBE-D3BJ).[6, 7] Monolayer simulation cells, including both unit cells and their supercells, had 20 Å vacuum space in the *c* direction, where the band structures and density of states of monolayers were calculated based on the unit cells and supercells, respectively (Fig. S3). 1H-WSe_2/1T-$SnSe_2$ and 1T'-WSe_2/1T-$SnSe_2$ HSs (~300 atoms with Γ k-point) were formed by joining two azimuthally aligned nanoribbon domains with periodic dislocation cores along the boundary as well as at least 25 Å vacuum space in the *b* direction. The initial structure was optimized until the force was below 0.02 eV/ Å, while keeping the coordinates in the *c* direction fixed.

Discussion Section

## Section 1: Apparent height measurement of core-shell structure
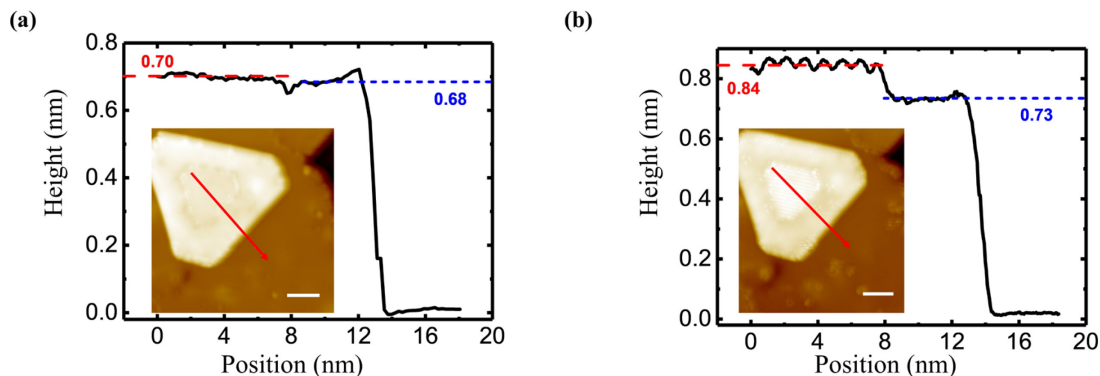
Figure S1. Bias-dependent apparent height measurements on the same core-shell structure. (a) Line profile measurement across the red trace on the inset STM image (V_s=2.0V, I_t=30pA). The apparent height for T'-WSe$_2$ and SnSe$_2$ are ~0.70nm and ~0.68nm, respectively. (b) Line profile measurement across the red trace on the inset STM image (V_s=1.6V, I_t= 30pA). Due to the convolution between morphology and electronic structures in STM measurements, the apparent heights of T'-WSe$_2$ and SnSe$_2$ are slightly modulated at a different sample bias. The ripples are related to the strip features of 1T'-WSe, which become more pronounced at this scanning condition. Scale bar: 5nm.

After SnSe$_2$ fully encloses WSe$_2$ island, a 2D lateral heterostructure with the inner WSe$_2$ core and outer SnSe$_2$ shell is effectively created. The apparent height measurements were conducted on the same core-shell structure on 1H-WSe$_2$/HOPG substrate (Fig. S1). The heights of monolayer T'-WSe$_2$ and T-SnSe$_2$ at 2V are ~0.70nm and ~0.68nm, respectively, which agree well with the typical monolayer thickness (0.6-0.7nm) of metal dichalcogenides from theoretical calculations,[8] as well as previous STM measurements of the same materials.[9, 10] However, it should be noted that the apparent height or the contrast in an STM image is convoluted between the film morphology and electronic structure, and thus can be influenced by the scanning conditions.[11] 1T'-WSe$_2$ core may appear slightly taller (brighter) or shorter (dimmer) than the surrounding SnSe$_2$ shell at different sample biases due to the contribution of electronic structures that are different between SnSe$_2$ and 1T'-WSe$_2$ (Fig. S1). Nevertheless, the apparent heights of the core measured at all biases are well below the thickness of bilayer metal dichalcogenides, which confirms the lateral geometry of the heterostructure.

Section 2: Identification of band edges in both experiment and theory

Charge transfer needs to be examined in the H-WSe$_2$:T-SnSe$_2$ heterostructure on HOPG. For the interfacial charge transfer with substrate, it is revealed by STS curves taken at locations far from the lateral boundary in both H-WSe$_2$ and T-SnSe$_2$ domains. Figure S2 (a) shows a representative STS curve taken on 1H-WSe$_2$. It illustrates an apparent bandgap of ~ 2.50 eV, consistent with the earlier reports.[12, 13] In the spectrum taken on SnSe$_2$ (Fig. S2(b)), there are three characteristic features labelled as VBM, CBM' and CBM. The difference between the two conduction bands is that CBM' originates from Γ point and CBM from M point of the Brillouin Zone. Note that the overestimation of 1H-WSe$_2$ bandgap by ~ 0.4 eV[14] and the stronger signal of CBM' in 1T-SnSe$_2$ are both related to the insensitivity of STS to states of larger parallel momentum ($k_\parallel$). In the Tersoff-Hamann model, tunneling current ($I \sim e^{-2\kappa d}$) depends

exponentially on the decay constant κ and tip sample distant d. Since $\kappa = \sqrt{\frac{2m\phi_b}{\hbar^2} + k_\parallel^2}$, tunneling into bands with smaller $k_\parallel$ such as Γ ($k_\parallel$=0) will be stronger than that into the bands of larger $k_\parallel$. ϕ_b is the effective tunneling barrier.[14, 15]

(a)

STS curve of 1H-WSe$_2$

(b)

STS curve of 1T-SnSe$_2$
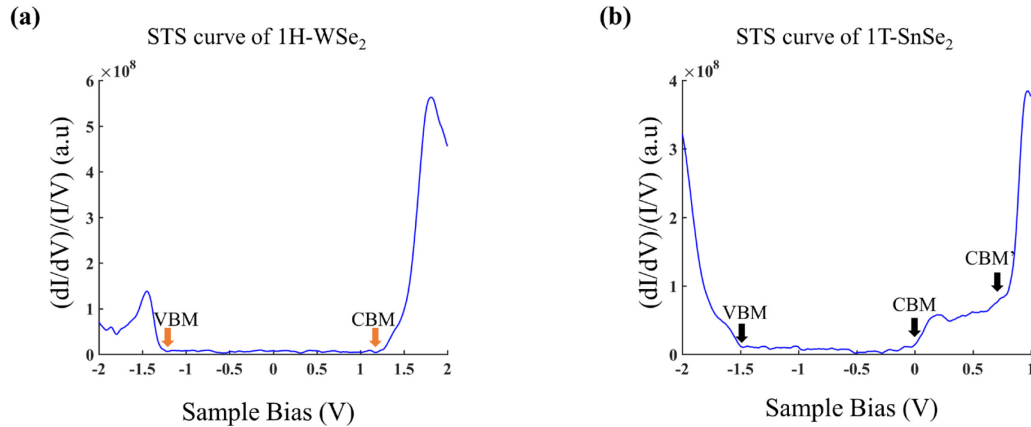
Figure S2. STS spectra taken on the interiors of 1H-WSe$_2$ and 1T-SnSe$_2$ on HOPG. (a) Representative normalized dI/dV (setpoint: V_s=2.0V, I_t=300pA) taken on the interior of 1H-WSe$_2$. Orange arrows mark the locations of band edges. The apparent bandgap is determined to be ~2.50 eV, with the VBM located at ~ -1.27 eV and CBM located at ~ 1.23 eV. (b) Representative normalized dI/dV (setpoint: V_s=-1.3V, I_t=200pA) taken on the interior of 1T-SnSe$_2$. There are three characteristic features labelled as VBM, CBM' and CBM. The identification of the band edges provides basis for the tracking of band bending in Fig. 2(a) and (b).

(a)

(b)

(c)
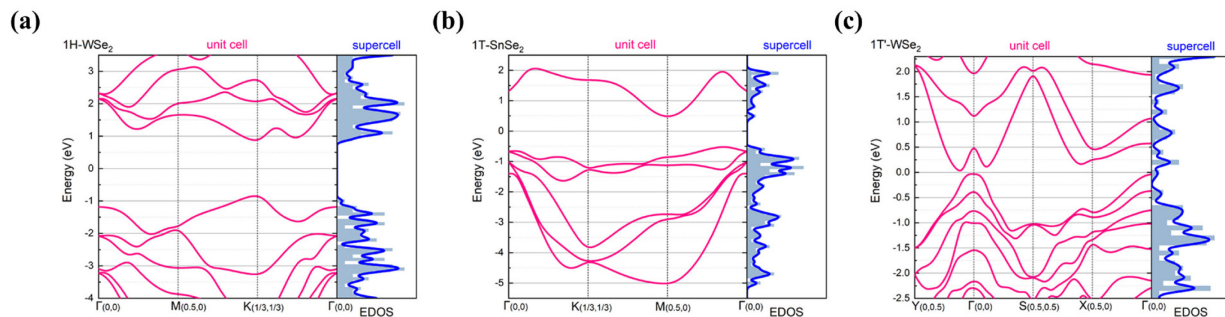
Figure S3. Comparison of electronic band structure calculation of monolayer TMD based on the unit cell and density of states (DOS) calculation of monolayer TMD based on the supercell. (a) 1H-WSe$_2$ (3-atom unit cell with 15×15×1 k-mesh and 8×7×1 supercell with Γ k-point). (b) 1T-SnSe$_2$ (3-atom unit cell with 16×16×1 k-mesh and 11×6×1 supercell with Γ k-point). (c) 1T'-WSe$_2$ (6-atom unit cell with 8×15×1 k-mesh and 4×7×1 supercell with Γ k-point). The same DFT parameters as discussed in the methods were used. Band structure calculations of monolayer TMDs (left panel) agree well with previous studies[16-18] that reported underestimation of bandgap by PBE. The DOS calculations of supercells (right panel) are consistent with what is expected from the left panel, although only Γ was sampled, which provides basis for the identification of VBM, CBM and CBM' used in the heterostructure plots in Fig. 3(e) and Fig. S4. Although the bandgaps of 1H-WSe$_2$ and 1T-SnSe$_2$ monolayers derived using supercells (right panels) are consistent with that presented in Fig. 3(e), band alignment in the heterostructure involves shifting of the band edges with respect to the global fermi level due to charge transfer between the two domains and with the boundary.

Section 3: Comparison between calculated PDOS and STS spectra, and between simulated boundary structure and STM image

In the construction of (7:6) $1H\text{-}WSe_2$ to $1T\text{-}SnSe_2$ alignment, Se-terminated zigzag edge is considered the most likely termination for $1H\text{-}WSe_2$ due to the Se-rich environment during MBE growth,[19] and subsequent deposition of $SnSe_2$ yields a covalently bonded lateral heterojunction. The optimized boundary structure illustrates the formation of dislocations, marked by the red arrows in Fig. 3(c), that are centered along the (7:6) segment as guided by the red dashed lines. Nonetheless, with respect to the black dashed lines drawn along the high symmetry direction of top Se atoms (Fig. 3(b)), the dislocation core appears to be shifted away from the center, consistent with the STM image in Fig. 3(a). Note that the periodic bright dots observed in the STM image correspond to the top Se atoms of TMDs due to STM sensitivity to tip-sample distance.

To identify boundary electronic structures, projected density of states (PDOS) are compared among various locations at the boundary as well as within the domain interiors (Fig. 3(e)). Real space charge density plots in Fig. 3(b-d) further elucidate the origins of the boundary states, i.e., the one enclosed by the red box is dominated by dislocation cores, and the two states marked by the black and blue boxes contain contribution from the entire boundary with the latter carrying a higher weight at dislocation cores. This finding is in excellent agreement with the STS results in Fig. 2(c), which can be visualized by comparing the experimental band alignment in Fig. 2(d) with that extrapolated theoretically in Fig. S4. In the STS spectra displayed in Fig. 2(c), the acceptor-like state marked by the blue arrows is also slightly modulated by dislocations.
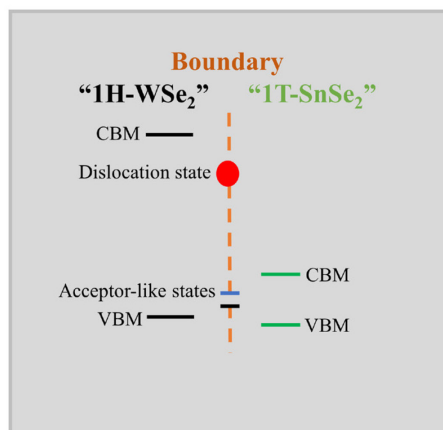
Figure S4. **Theoretically extrapolated band alignment from PDOS analysis in Fig. 3(e).** The relative peak locations agree with Fig. 2(d), where the acceptor-like states are near the VBMs and the dislocation state is above the CBM of $1T\text{-}SnSe_2$ and below the CBM of $1H\text{-}WSe_2$. The major differences from Fig. 2(d) are likely associated with the underestimation of bandgap by DFT, as shown in Fig. S3, and the charge transfer with substrate which was not considered in the DFT calculation. Note that band bending near boundary is not mapped since PDOS was only analyzed in the center of TMD domains and along the boundary in Fig. 3(e).

Section 4: Structure description of 1T'-WSe₂/1T-SnSe₂ boundary
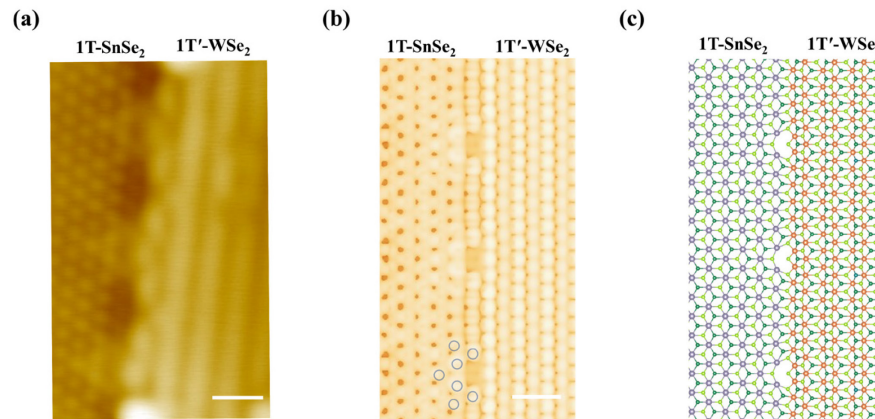
Figure S5. Structural comparison for 1T'-WSe₂/1T-SnSe₂ boundary. (a) STM image (V$_s$=1.0V, I$_t$=100pA), (b) Simulated STM image of the heterostructure at 1V, (c) DFT calculated atomic structure. Scale bar: 1nm.

For clarification regarding the structure of 1T'-WSe₂/1T-SnSe₂ boundary, a new figure with the STM image, DFT calculated structure and image separately presented is included above, along with some details to guide the comparison: (i) The periodicity of dislocation core (6 times SnSe₂ lattice constant) is consistent between experimental observation and theoretical calculation (Fig.S5(a-c)). (ii) The protrusions observed on the 1T-SnSe₂ side should be mostly contributed by top Se atoms due to the surface sensitivity of STM. On the 1T'-WSe₂ side, the stripe features are dominated by the top Se and the dimerized W rows, consistent with previous reports.[20] The DFT calculated structure and image align well with these features (Fig. 3(f,g)). (iii) Near the dislocation core, a star-like pattern is observed in the experiment, which is also revealed in the simulated image as labeled by the blue circles. This likely originates from the DOS contribution of the dislocations.

Section 5: An additional source of lattice misalignment between merging SnSe₂ domains
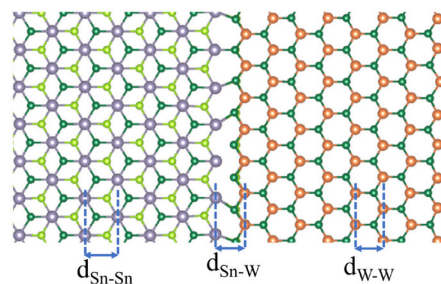
Figure S6. Optimized atomic structure of 1H-WSe₂/1T-SnSe₂ boundary by DFT. Distance between the two domains is optimized at the junction, but it differs from the internal bond lengths within each domain, which can be visualized in the projected metal-metal distance (marked by blue dashed lines): d_{Sn-Sn} (0.329nm) > d_{Sn-W} (0.293nm) > d_{W-W} (0.286nm). This structure difference between the boundary and the shell constitutes an additional source to the lattice misalignment when two adjacent SnSe₂ domains merge into each other.

Section 6: Complications in MBE deposition and discussion of sample scalability

(a) **(b)**
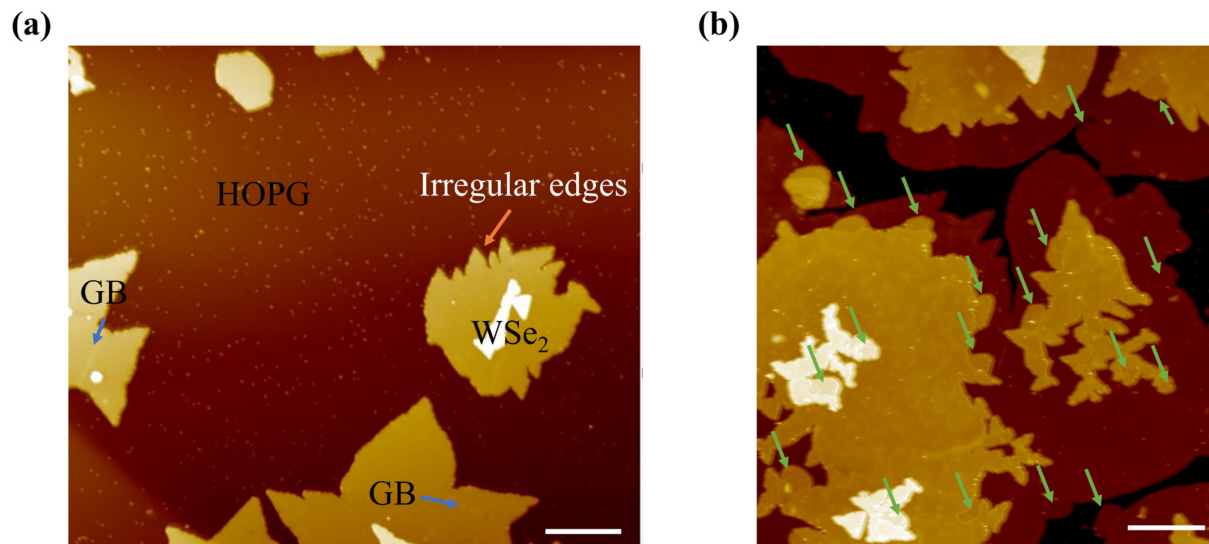
Figure S7. Complications in MBE growth of WSe₂. (a) Large scale STM image (Vs= 2.0V, I_t= 30pA) of WSe$_2$ on HOPG before deposition of SnSe$_2$. The growth is not layer by layer with the formation of 2nd or even 3rd layer before the completion of 1st layer. Irregular edges can be found on some large WSe$_2$ islands, arising from the limited edge diffusion. Blue arrows mark the locations of grain boundaries (GB). (b) Large scale STM image (Vs= 1.8V, I_t= 30pA) of SnSe$_2$/WSe$_2$ on HOPG. SnSe$_2$ and WSe$_2$ domains can be differentiated by the color contrast. SnSe$_2$, labeled by the green arrows, always emerge at the bottom edge of WSe$_2$. No stand-alone SnSe$_2$ islands are observed, suggesting that Sn and Se adatoms have reasonable long diffusion length to explore the surface potential landscape and find the preferred nucleation sites. Scale bar: 50nm.

Unlike chemical vapor deposition (CVD), it remains challenging to achieve a large single crystalline domain of WSe$_2$ on a vdW substrate by MBE. MBE operates under ultrahigh vacuum (UHV) environment and the sticking coefficient of Se is significantly lowered,[21] which limits the growth temperature and therefore the diffusion length of metal adatoms on the surface and along the edge. This results in smaller domain size and less compact shape of WSe$_2$ in comparison to CVD growth.[21, 22] At our typical growth conditions, the "larger" WSe$_2$ islands are often consisted of multiple domains with domain boundaries (Fig. S7(a)). Irregular edges (Fig. S7(a)) could also appear due to the considerably large edge diffusion barrier.[23] When SnSe$_2$ domains nucleated on these irregular edges encounter with each other and coalesce, there is a high chance to develop grain boundaries within SnSe$_2$ due to the arbitrary azimuthal alignment. Formation of grain boundaries in either the shell or the core structure could release the strain that is created during the process of shell coalescing, thus reduce the possibility to transform WSe$_2$ domains. As a result, in our experiment the 1T' phase is typically observed in the compact single crystalline domains as shown in Fig.1(c-e). CVD has demonstrated the success to grow large monolayer WSe$_2$ with well-defined shapes/edges,[24] which could help overcome the difficulties in the MBE experiment.

The diffusion length appears to be reasonably long for Sn and Se atoms. So far, we have not observed a stand-alone SnSe$_2$ island that is not attached to a WSe$_2$ edge, including those landing on top of WSe$_2$, as illustrated in the early-stage growth of SnSe$_2$ (Fig. S7(b)). This suggests that the incoming Sn and Se adatoms have long enough diffusion length to explore the WSe$_2$ surface and find preferred nucleation sites at WSe$_2$ edges, favoring the formation of lateral heterojunctions. It is likely associated

with the small Schwoebel barrier (additional barrier for adatoms to diffuse down a step) due to weak vdW interaction along the vertical direction.

Section 7: Topological properties of 1T'-WSe$_2$

The spatial extension of the topological edge state does not vary between the smooth and "rough" boundaries, as discussed in the main text. Additionally, investigations on various locations of the arc-like features on the 1T'-WSe$_2$/1T-SnSe$_2$ boundary, arising from dislocation cores, also indicate the persistence of the edge state despite slightly modulated peak intensity (Fig. S8).
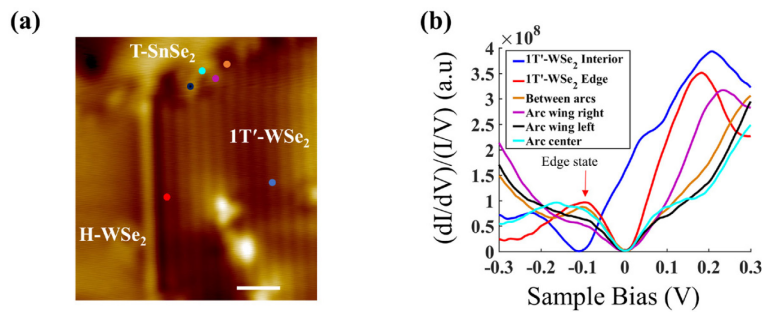
Figure S8. Topological edge state on the 1T'-WSe$_2$/1T-SnSe$_2$ boundary with structural perturbations from misfit dislocations. (a) STM image of the partially converted WSe$_2$ island (V$_s$=2V, I$_t$=30pA) on 1H-WSe$_2$/HOPG substrate. The zoomed-out image of the same area is shown in Fig. 1(c). (b) Normalized dI/dV (setpoint: V$_s$=0.5V, I$_t$=200pA) spectra taken on the interior of 1T'-WSe$_2$, the smooth edge between H- and T'-WSe$_2$, and on various locations of the T'-WSe$_2$/T-SnSe$_2$ boundary. Locations of the spectra are marked using dots of respective colors in (a). Regardless of boundary morphology and local structural perturbation, the edge state, as marked by the red arrow, persists with only slight modification of intensity. Scale bar: 2nm.

Electronic Supplementary Material (ESI) for Materials Horizons.

References:

1.   J. VandeVondele, M. Krack, F. Mohamed, M. Parrinello, T. Chassaing and J. Hutter, *Comput. Phys. Commun.*, 2005, **167**, 103-128.
2.   J. Hutter, M. Iannuzzi, F. Schiffmann and J. VandeVondele, *Wiley Interdisciplinary Rev.-Comput. Mol. Sci.*, 2014, **4**, 15-25.
3.   S. Goedecker, M. Teter and J. Hutter, *Phys. Rev. B*, 1996, **54**, 1703-1710.
4.   M. Krack, *Theor. Chem. Acc.*, 2005, **114**, 145-152.
5.   J. VandeVondele and J. Hutter, *J. of Chem. Phys.*, 2007, **127**, 114105.
6.   S. Grimme, S. Ehrlich and L. Goerigk, *J. of Comput. Chem.*, 2011, **32**, 1456-1465.
7.   Y. K. Zhang and W. T. Yang, *Phys. Rev. Lett.*, 1998, **80**, 890-890.
8.   F. A. Rasmussen and K. S. Thygesen, *The J. of Phys. Chem. C*, 2015, **119**, 13169-13183.
9.   W. Chen, X. D. Xie, J. Y. Zong, T. Chen, D. J. Lin, F. Yu, S. E. Jin, L. J. Zhou, J. Y. Zou, J. Sun, X. X. Xi and Y. Zhang, *Sci. Rep.*, 2019, **9**, 2685.
10.   Z. Shao, Z. G. Fu, S. Li, Y. Cao, Q. Bian, H. Sun, Z. Zhang, H. Gedeon, X. Zhang, L. Liu, Z. Cheng, F. Zheng, P. Zhang and M. Pan, *Nano Lett.*, 2019, **19**, 5304-5312.
11.   T. Le Quang, V. Cherkez, K. Nogajewski, M. Potemski, M. T. Dau, M. Jamet, P. Mallet and J. Y. Veuillen, *2D Mater.*, 2017, **4**, 035019.
12.   H. Liu, J. Chen, H. Yu, F. Yang, L. Jiao, G. B. Liu, W. Ho, C. Gao, J. Jia, W. Yao and M. Xie, *Nat. Commun.*, 2015, **6**, 8180.
13.   Y. L. Huang, Y. Chen, W. Zhang, S. Y. Quek, C. H. Chen, L. J. Li, W. T. Hsu, W. H. Chang, Y. J. Zheng, W. Chen and A. T. Wee, *Nat. Commun.*, 2015, **6**, 6298.
14.   C. Zhang, Y. Chen, A. Johnson, M. Y. Li, L. J. Li, P. C. Mende, R. M. Feenstra and C. K. Shih, *Nano Lett.*, 2015, **15**, 6494-6500.
15.   Y. M. Zhang, J. Q. Fan, W. L. Wang, D. Zhang, L. L. Wang, W. Li, K. He, C. L. Song, X. C. Ma and Q. K. Xue, *Phys. Rev. B*, 2018, **98**.
16.   H. Liu, P. Lazzaroni and C. Di Valentin, *Nanomaterials*, 2018, **8**, 481.
17.   J. M. Gonzalez and I. I. Oleynik, *Phys Rev B*, 2016, **94**, 125443.
18.   X. Qian, J. Liu, L. Fu and J. Li, *Science*, 2014, **346**, 1344-1347.
19.   S. S. Wang, Y. M. Rong, Y. Fan, M. Pacios, H. Bhaskaran, K. He and J. H. Warner, *Chem. Mater.*, 2014, **26**, 6371-6379.
20.   R. Sankar, G. Narsinga Rao, I. P. Muthuselvam, C. Butler, N. Kumar, G. Senthil Murugan, C. Shekhar, T.-R. Chang, C.-Y. Wen, C.-W. Chen, W.-L. Lee, M. T. Lin, H.-T. Jeng, C. Felser and F. C. Chou, *Chem. Mater.*, 2017, **29**, 699-707.
21.   T. H. Choudhury, X. Zhang, Z. Y. Al Balushi, M. Chubarov and J. M. Redwing, *Annu. Rev. of Mater. Res.*, 2020, **50**, 155-177.
22.   G. S. Bales and D. C. Chrzan, *Phys. Rev. Lett.*, 1995, **74**, 4879-4882.
23.   R. Yue, Y. Nie, L. A. Walsh, R. Addou, C. Liang, N. Lu, A. T. Barton, H. Zhu, Z. Che, D. Barrera, L. Cheng, P.-R. Cha, Y. J. Chabal, J. W. P. Hsu, J. Kim, M. J. Kim, L. Colombo, R. M. Wallace, K. Cho and C. L. Hinkle, *2D Mater.*, 2017, **4**, 045019.
24.   Y. Zhang, Y. Yao, M. G. Sendeku, L. Yin, X. Zhan, F. Wang, Z. Wang and J. He, *Adv. Mater.*, 2019, **31**, e1901694.